The Astrophysical Journal, 904:114 (12pp), 2020 December 1 https://doi.org/10.3847/1538-4357/abc340

The Galaxy "Missing Dark Matter" NGC 1052-DF4 is Undergoing Tidal Disruption

Mireia Montes[1], Raúl Infante-Sainz[2,3], Alberto Madrigal-Aguado[2,3], Javier Román[4], Matteo Monelli[2,3], Alejandro S. Borlaff[5], and Ignacio Trujillo[2,3]
[1] School of Physics, University of New South Wales, Sydney, NSW 2052, Australia; mireia.montes.quiles@gmail.com
[2] Instituto de Astrofísica de Canarias, c/ Vía Láctea s/n, E-38205—La Laguna, Tenerife, Spain
[3] Departamento de Astrofísica, Universidad de La Laguna, E-38205—La Laguna, Tenerife, Spain
[4] Instituto de Astrofísica de Andalucía (CSIC), Glorieta de la Astronomía, E-18008 Granada, Spain
[5] NASA Ames Research Center, Moffett Field, CA 94035, USA
Received 2020 September 29; revised 2020 October 15; accepted 2020 October 19; published 2020 November 26

Abstract

The existence of long-lived galaxies lacking dark matter represents a challenge to our understanding of how galaxies form. Here, we present evidence that explains the lack of dark matter in one such galaxy: NGC 1052-DF4. Deep optical imaging of the system has detected tidal tails in this object caused by its interaction with its neighboring galaxy NGC 1035. As stars are more centrally concentrated than dark matter, tidal stripping will remove a significant percentage of dark matter before affecting the stars of the galaxy. Only $\sim$7% of the stellar mass of the galaxy is in the tidal tails, suggesting that the stars of NGC 1052-DF4 are only now starting to be affected by the interaction, while the percentage of remaining dark matter is $\lesssim$1%. This naturally explains the low content of dark matter inferred for this galaxy and reconciles these types of galaxies with our current models of galaxy formation.

Unified Astronomy Thesaurus concepts: Dark matter (353); Galaxy formation (595); Galaxy interactions (600)

1. Introduction

Dark matter (DM) is a key constituent in current models of galaxy formation and evolution. In fact, without the presence of DM, the primordial gas would lack enough gravitational pull to start collapsing and forming new galaxies. Because this DM is thought to interact mostly gravitationally, its presence can only be inferred from its effect on the visible matter (e.g., Freeman 1970; Rubin & Ford 1970).

Although transient, DM-free, stellar aggregations (also called Tidal Dwarf Galaxies) have been known for some time (see, e.g., Duc et al. 2000; Lelli et al. 2015; Ploeckinger et al. 2015, 2018), the existence of long-lived nonisolated galaxies lacking DM would be a challenge to the current galaxy formation paradigm. For this reason, the recent report of two old potentially stable galaxies with low (or null) DM content, [KKS2000]04 (also known as NGC 1052-DF2) and NGC 1052-DF4 (van Dokkum et al. 2018, 2019, hereafter vD19), has triggered an intense debate about the nature of these objects. While in the case of [KKS2000]04 (NGC 1052-DF2) its unusual properties can be simply resolved if the object is located at 13 Mpc (instead of the originally assumed 20 Mpc, see e.g., Trujillo et al. 2019), the low velocity dispersion of the globular clusters (GCs) of NGC 1052-DF4 is compatible with the absence of DM, even at a closer distance (13.5 Mpc, Monelli & Trujillo 2019).

An appealing alternative to explain the low DM content of NGC 1052-DF4 is that this galaxy is undergoing tidal stripping (e.g., Ogiya 2018; Jackson et al. 2020; Łokas 2020; Macciò et al. 2020; Nusser 2020; Yang et al. 2020). In fact, NGC 1052-DF4 is very close both in velocity ($\Delta v \sim 180$ km s^{-1}) and in spatial projection ($\Delta R \sim 4'$) to the galaxy NGC 1035. If NGC 1052-DF4 is undergoing tidal disruption, this could explain the apparent lack of DM as this is preferentially stripped over the stars of the galaxy or its GC system, due to its more extended spatial distribution (Smith et al. 2013, 2016).

In this paper, we explore the tidal stripping scenario and whether it can explain the "lack" of DM observed in NGC 1052-DF4. We explore this scenario in two ways. First, we explore the spatial distribution of the GCs in NGC 1052-DF4. If NGC 1052-DF4 is being tidally stripped by NGC 1035, their stripped GCs would be placed along the orbit traced by the satellite. Therefore, exploring how the spatial distribution of GCs in NGC 1052-DF4 is can give us clues about the present state of the galaxy.

Second, we obtained very deep imaging of NGC 1052-DF4 in order to search for any signs of tidal interactions in the stellar light around this galaxy (see also Müller et al. 2019). Tidal effects in dwarf galaxies have been studied in simulations (e.g., Johnston et al. 1996; Read et al. 2006; Peñarrubia et al. 2008, 2009), and they have found that if, for example, tidal tails are present in the outer parts of this galaxy, their shape and direction can provide information of the current orbit of the satellite (e.g., Johnston et al. 2002; Klimentowski et al. 2009).

In this paper, we will demonstrate that both the GCs and the stellar distribution of NGC 1052-DF4 are in agreement with the tidal stripping scenario. We will also discuss how this stripping scenario explains the apparent "lack" of DM, making this galaxy perfectly compatible with the current galaxy formation paradigm. All magnitudes in this work are given in the AB magnitude system.

2. Data

The data used in this paper come from three different facilities: the Hubble Space Telescope (HST) and two ground-based telescopes: the Gran Telescopio Canarias (GTC) and the IAC80 telescopes. We describe the details of each observation on what follows.

2.1. HST Imaging

NGC 1052-DF4 was observed with the HST ACS Wide-Field Channel (WFC) as part of the programmes GO-14644 and GO-15695 (PI: van Dokkum). We retrieved the data from

the MAST archive.[6] The observations consist of a total of four orbits in the F606W band and eight in the F814W band. The total exposure time is 8240 s for the F606W and 16,760 s in F814W.

To obtain the final coadded images, we follow the approach detailed below. The individual frames were precalibrated in a standard way, i.e., bias- and dark-current-subtracted, flat-fielded, and charge transfer efficiency (CTE)-corrected producing `flc` files. A preliminary luminance coadd using the images of both filters was made using `Astrodrizzle` (Gonzaga et al. 2012) with a median constant sky subtraction. We used this first coadd to create a deep master mask using `NoiseChisel` (Akhlaghi & Ichikawa 2015; Akhlaghi 2019), later applied to each individual frame in order to derive a more robust sky background. This deep master mask was manually expanded to include any remaining light from NGC 1052-DF4 and other large sources in the field of view, and then drizzled to the field of view of each individual exposure. For each one of them, we subtract a robust median sky-background level (using bootstrapping to avoid the effect of outliers and cosmic rays) from masked frames (see Borlaff et al. 2019 for further details).

At this point, the rough astrometry provided by the headers of the `flc` files was refined using the `TweakReg` utility. After this, we derived the final coadd for the images with `Astrodrizzle` into astrometrically corrected drizzled images with the F814W and F606W filters. The relevant drizzling parameters used are `pixfrac=1`, `kernel=lanzcos3`, and `combine type=-iminmed`. Note that the `combine type` option, `iminmed`, is generally the same as the median, except when the median is significantly higher than the minimum good pixel value. In those cases, `iminmed` will choose the minimum value. The final coadd of the images still shows a significant gradient across the detector, consistent in both filters, lower close to the gap between the CCDs. To mitigate this problem, we used `NoiseChisel` to generate a final sky-background model for the coadded images, following the optimized methodology for the detection of the low surface brightness wings of extended sources.[7] The optimal configuration was set at `tilesize = 300,300`, `interpnumngb = 3`. As a final step, after this background model has been subtracted, we readjust the median sky-background level by a constant once again using the deep master mask.

We take advantage of these high-resolution HST/ACS observations, together with the photometry from the GTC HiPERCAM data (see Section 2.2.1) to characterize the GC population of NGC 1052-DF4.

2.2. Deep Ground-based Imaging

The study of low surface brightness light in deep images is extremely challenging. It is not enough to have very deep data, but a careful data reduction is crucial. In fact, it is common to find "dips" around the brightest extended objects in very deep surveys (see, e.g., CFHTLS and the HSC-SSP DR1; Goranova et al. 2009; Aihara et al. 2018) due to aggressive sky subtraction. In addition, the study of diffuse and extended objects is susceptible to biases due to flat-field inaccuracies and the scattered light from bright stars, to name a few.

NGC 1052-DF4 was observed with the GTC and the IAC80 telescope. Most of the reduction steps are common for both data sets and, therefore, described in the following. Specifics for each of the telescopes are discussed later. The aim of this reduction process is to correct all systematics effects introduced by the instrument/telescope as well as to calibrate the data. The whole reduction process was done within a controlled and enclosed environment as described in Akhlaghi et al. (2020).

Deep observations require an observing strategy that produces a background as flat as possible around our galaxy target. Another key step is the dithering pattern. For this work, we followed the dithering strategy in Trujillo & Fliri (2016). In short, this consists of a dithering pattern with large steps (typically the size of the source under investigation) and whenever possible rotation of the camera. This ensures we achieve the flat background required for our goals.

Bias frames were taken the same night of the observations as part of the different observing programs. The master bias frames were created as the sigma-clipped (3σ) mean and subtracted from the original images.

Dome flats are not suitable for our goals due to inhomogeneities in the dome illumination that can result in gradients across the image. Consequently, the flat-field frames derived here are based on the same science exposures obtained for this work. To solve this, the flat-field correction was performed in two steps. As the bias-corrected CCD frames present steep gradients,[8] we first stack each bias-corrected image after normalizing them by its 3σ-clipped mean. This produces a rough master flat-field frame that is used to correct the CCD frame. These corrected CCD images were used to build an object mask using `NoiseChisel`'s detection maps. Again, for each CCD, the masked and normalized images are combined to create the final, and more accurate, master flat-field frames for each band.

We, then, performed the astrometric calibration of the different frames. We used the `Astrometry.net` software (Lang et al. 2010) to produce an approximate astrometric solution, later refining it with `scamp` (Bertin 2006). Later, we performed the sky-background correction by masking all signal pixels detected with `NoiseChisel` for each frame. The remaining pixels are used to compute a first-degree 2D polynomial fit that is then subtracted from the entire frame. This ensures the correction of any remaining gradient while preserving local low surface brightness structures.

Once all frames were corrected of all systematic effects and in a common astrometric solution, they were resampled into a common grid using `SWarp` (Bertin 2010) and stacked using a 3σ-clipped mean into a final image, one per filter. The photometric calibration of both sets of images, HiPERCAM and IAC80, was done using SDSS DR12 (Alam et al. 2015).

2.2.1. GTC HiPERCAM Images

Deep multiband imaging with GTC was requested through Director Discretionary Time to observe NGC 1052-DF4 with HiPERCAM. HiPERCAM (Dhillon et al. 2018) is a quintuple-beam, high-speed astronomical imager able to obtain images of celestial objects in five different filters (u, g, r, i, z) simultaneously. The image area of each of the five CCDs is 2048×1024 pixels ($2\farcm7 \times 1\farcm4$; 1 pixel $=0\farcs08$) divided into four channels of 1024×512 pixels. NGC 1052-DF4 was observed between 2019 September 4 and 8. During these

[6] https://mast.stsci.edu/portal/Mashup/Clients/Mast/Portal.html

[7] Gnuastro 2.3 Tutorial—Detecting large extended targets: https://www.gnu.org/s/gnuastro/manual/html_node/Detecting-large-extended-targets.html.

[8] This is due to illumination inhomogeneities as well as fringing, particularly for the GTC HiPERCAM z band.

observations, there was a problem with the electronics of the *i*-band CCD, making it impossible to use this band. The average seeing of the images was 1.″1.

For HiPERCAM, the standard calibration of each individual frame, i.e., bias and flat-field correction, was performed in each channel of the CCD. After the flat-field correction, we assembled each set of four channels into a single image per filter. To do this, a fine gain correction is done by computing the average value along the adjacent pixels for the different channels.

We obtained ∼55 exposures per filter using a constant exposure time of 106 s per frame. The different exposures that went into the final images were visually inspected and rejected if rejecting those with low-quality or strong gradients were still present. The final exposure times in the innermost $R < 1'$ of the images are 1.6, 1.7, 1.5, and 1.7 hr for the u, g, r, and z bands, respectively.

Unfortunately, the modest field of view of HiPERCAM is similar to the size of the galaxy (with a diameter of ∼1.′5). This precludes a reliable sky subtraction and, therefore, the analysis of the extended low surface brightness emission around NGC 1052-DF4. Consequently, even though the GTC data are very deep, we only used them to study the GC system around NGC 1052-DF4 (which, being point-like sources, are not significantly affected by the sky subtraction). The point-like source limiting magnitudes (5σ in 2″ diameter apertures) are $m_u = 27.11 \pm 0.06$, $m_g = 26.98 \pm 0.07$, $m_r = 26.44 \pm 0.07$, and $m_z = 24.81 \pm 0.10$ mag.

2.2.2. IAC80

In order to explore the distribution of light around NGC 1052-DF4 and NGC 1035, we use the IAC80 telescope. The IAC80 telescope is an 82 cm telescope located at the Teide Observatory in Tenerife. The camera currently installed at its Cassegrain primary focus, and used here, is CAMELOT2 (the Spanish acronym of the "Teide Observatory Light Improved Camera"). It contains an E2V 2048 × 2048 back-illuminated chip with a pixel scale of 0.″336 per pixel corresponding to a 10.′4 × 10.′4 field of view. This field of view is enough to get a reliable sky estimation around NGC 1052-DF4. NGC 1052-DF4 was observed with CAMELOT2 between 2019 December 19 and 2020 February 20 in the g, r, and i bands. The final exposure times are 22.33, 23.33, and 15.66 hr for the g, r, and i bands respectively. The surface brightness limits of these images are $\mu_g = 29.8$, $\mu_r = 29.3$, and $\mu_i = 28.8$ mag arcsec^{-2} (3σ; 10″ × 10″ boxes). They were estimated by measuring the rms of the final masked images by randomly placing 3000 boxes of 10″ × 10″ across the images.

Figure 1 shows the 13.′3 × 13.′3 region around NGC 1052-DF4 taken with the IAC80 telescope. In the figure, we have also plotted the field of view of the IAC80/CAMELOT2, GTC/HiPERCAM, and HSC/ACS cameras for ease of comparison.

2.2.3. PSF Modeling and Bright Star Subtraction of the IAC80 Images

A key aspect in low surface brightness science is to remove the scattered light field produced by the brightest of objects of the images. To do this, an accurate characterization of the point-spread function (PSF) of the images is required. As we are only studying the distribution of light around NGC 1052-DF4 in the IAC80 images, this was done only for these images.

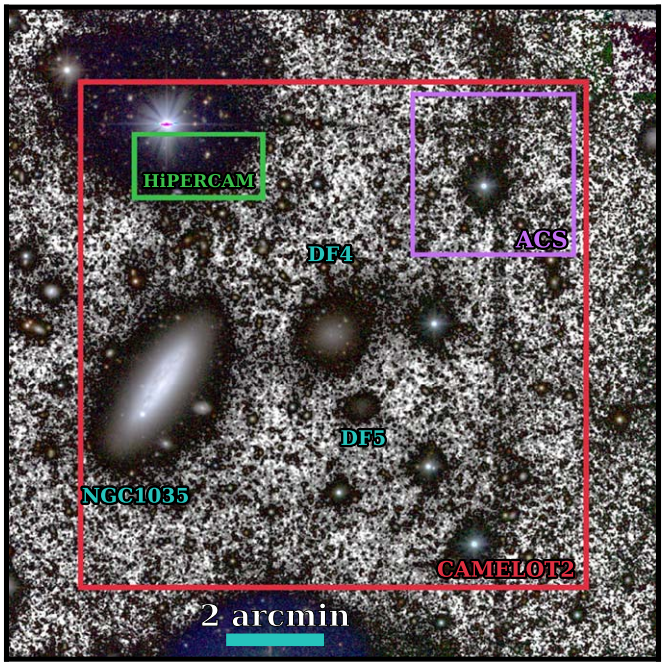

Figure 1. We show a 13.′3 × 13.′3 region around NGC 1052-DF4 imaged with the IAC80 telescope. The figure is a composite of an RGB color image using the g, r, and i IAC80 bands and a black and white $g + r + i$ image for the background. The figure highlights the main galaxies in the field of view: NGC 1052-DF4 and their neighbors NGC 1035 and NGC 1052-DF5. The fields of view of the different cameras used in this paper are overplotted. The surface brightness limit of this composite image is equivalent to $\mu_r \sim 29.9$ mag arcsec^{-2} (3σ; 10″ × 10″ boxes). North is up, east is left.

To build the extended ($R = 7.'5$) PSF models of the IAC80 telescope, we followed the methodology outlined in Román et al. (2019) and Infante-Sainz et al. (2020). The outermost regions of the PSFs were obtained through dedicated observations of bright stars with magnitudes between 3.2 and 4.8 mag, in the V band. The exposure times vary with the star magnitude and the observed band between 7 and 22 s. The observations of the bright stars were conducted with a large dithering pattern in order to cover the entire field of view of the camera. Individual frames were masked to avoid the contamination of background sources and finally combined to create the outer parts of the PSF models.

Because we only use bright stars to build this model, the final PSF models are saturated in the center. However, as the goal is to eliminate the contribution of the outer parts of bright stars surrounding NGC 1052-DF4, we did not derive the inner parts of the PSF model. We fit and subtracted eight bright stars in the field of view of the camera that could affect our photometry. To subtract the stars in our images, we follow the steps outlined in Román et al. (2019).

3. The Spatial Distribution of the Globular Cluster System around NGC 1052-DF4

Globular clusters (GCs) are thought to form in the episodes of intense star formation that shaped galaxies (see Brodie & Strader 2006 and references therein). Their typical masses ($10^{4-6} M_\odot$) and compact sizes (half-light radii of a few parsecs; Harris 1996) make them easily observable in external galaxies and, therefore, good tracers of the properties of their host

system even at large radial distances, unlike stellar dynamics studies that are limited to the inner regions of galaxies.

The spatial distribution of the GC system of a galaxy might reveal clues about its present state. For instance, in an accretion event, the stripped material is placed along the orbit of the parent satellite galaxy, forming tidal streams (e.g., Toomre & Toomre 1972; Johnston et al. 1996). Therefore, during this process, the stripped GCs will also align along the orbit (e.g., Mackey et al. 2010; Hughes et al. 2019) and, consequently, their observed spatial distribution can indicate the direction of this orbit.

vD19 identified seven GCs associated with NGC 1052-DF4 by confirming them spectroscopically after a first selection based on their HST F606W − F814W color. In this section, we use our deep HiPERCAM imaging to identify additional GC candidates and determine the spatial distribution of the GCs of NGC 1052-DF4. The goal is to explore whether the GCs align through a particular direction, which could indicate that NGC 1052-DF4 is undergoing tidal stripping or, on the contrary, the GCs are more spherically distributed around NGC 1052-DF4 as it would be expected if the galaxy is in isolation.

3.1. GCs Selection

The task of identifying GCs in galaxies is nontrivial. The uncertain level of foreground and background contamination limits its utility in characterizing the overall GC system of the host galaxy with a large degree of confidence. A common technique for identifying GCs in galaxy systems is to use their colors. However, recent works have shown the increased effectiveness of identifying GCs using more information from their spectral energy distributions (e.g., Montes et al. 2014; Muñoz et al. 2014).

For this reason, in order to identify more GC candidates in NGC 1052-DF4, we use the $(u - r)$–$(r - z)$ color–color diagram, as described in Taylor et al. (2017). In this case, the effectiveness of this selection criterion is based in the inclusion of the u band, which allows a cleaner separation of metal-poor GCs from the foreground stars of our Galaxy. The presence of hot horizontal branch stars, contributing to the flux in the u band, in these metal-poor GCs will make them bluer in $u - r$ than foreground stars for a given $r - z$.

For a preliminary selection, we took advantage of the high spatial resolution of HST to preselect potential GCs based on their morphology (FWHM and ellipticity) and F606W magnitude, $m_{\rm F606W}$. This selection was modeled upon the properties of the confirmed GCs in vD19. First, we run `SExtractor` (Bertin & Arnouts 1996) on the HST images in dual mode using F814W as the detection image. We also ran `SExtractor` in the HiPERCAM images of NGC 1052-DF4 using in this case the r image as our detection image. Once the catalogs for the different instruments, HST and HiPERCAM, are obtained, we matched them based on their position in the sky.

The initial GC selection consists of objects that simultaneously fulfill the following properties: $0\farcs1 <$ FWHM $< 0\farcs2$, $0 <$ ellipticity < 0.2 and $20 < m_{\rm F606W} < 25$ mag. This observed magnitude range corresponds to the absolute magnitude range $-10.65 < M_{\rm F606W} < -5.65$ if the galaxy is at 13.5 Mpc or $-11.5 < M_{\rm F606W} < -6.5$ if the galaxy is at 20 Mpc. The aim of this selection is to find GCs that are similar to the confirmed GCs while allowing for sources that might have been missing from the spectroscopic-based sample. Figure 2 shows the histograms of the FWHM, ellipticity, and $m_{\rm F606W}$ of all the sources detected with `SExtractor` (gray), the confirmed GCs in vD19 (magenta), and the GC candidates based on our preliminary selection (mint green). Twenty objects fall within this preselection, including the seven objects in vD19.

The next step is to narrow down the selection based on the colors of the GCs. Figure 3 shows the $(u - r)$−$(r - z)$ color–color diagram for the preselected GC candidates (mint green) from our preliminary selection. We highlighted the seven GCs in vD19 in magenta. As seen in Figure 3, the confirmed GCs fill a very narrow space in the color–color diagram, and therefore, we further narrowed down the initial selection to objects with $1.5 < u - r < 2.2$ and $0.55 < r - z < 0.75$, shown as the red box in Figure 3. These ranges in color are based on the $\pm 3\sigma$ around the median colors of the confirmed GCs highlighted in magenta, with σ being their dispersion in color. Using this color selection, our final sample consists of a total of 11 GCs, 4 new candidates in addition to the confirmed GCs in vD19. The radius containing half of the GCs is $\sim 155''$, 9 times larger than the R_e of the stellar light ($17''$; vD19).

The new GC candidates reported here are located to the West of NGC 1052-DF4, the side facing away from NGC 1035, which is less likely to be contaminated by the GC system of the disk galaxy. In addition, we expect very low GC contamination from this low-mass disk galaxy. Using the Milky Way as a reference, and the correlation between the size of the GC system and the stellar mass of the host (Forbes 2017), we expect NGC 1035 to have half of their GCs contained within a radius of <4 kpc or $61''/42''$ (Hudson & Robison 2018) at 13.5/20 Mpc, respectively. For reference, the projected distance between the centers of the galaxies is $222''$.

The coordinates and magnitudes of all the objects are listed in Table 1. The magnitudes are corrected by the extinction of our Galaxy: $A_v = 0.11$, $A_g = 0.08$, $A_r = 0.06$, $A_z = 0.03$, $A_{\rm F606W} = 0.06$, and $A_{\rm F814W} = 0.04$.

3.2. The Distribution of GCs around NGC 1052-DF4

In this section, we address the spatial distribution of the GCs in NGC 1052-DF4 in order to obtain clues about the interaction state of the galaxy. As mentioned before, in an accretion event, the stripped material (stars and GCs) will be deposited along the orbit of the parent satellite. In Figure 4, we show an RGB image created using the HiPERCAM g, r, and z bands. The highlighted sources are the confirmed GCs from vD19 (magenta) and the new candidates obtained in the previous section (mint green). The GCs tend to align in a particular axis along the galaxy.

In order to derive this axis, we use `scipy.odr` to perform an orthogonal distance regression to all the GCs, confirmed and candidates. We use the orthogonal distance regression as we are interested in calculating the orthogonal distance to the axis instead of predicting the value of Y for any given X. The range of possible axes, i.e., directions of the orbit, will be given by the slope of the regression and its error. This is indicated by the blue-shaded region in Figure 4. This region encompasses 68% of the axes compatible with the GC distribution. One of the GCs, marked by a dashed circle, might be associated with NGC 1052-DF5 given its proximity to this galaxy and, consequently, might be biasing the computed axis. Taking that into consideration, we computed again the range of possible axes but this time removing this GC, shown by the region enclosed by the dashed blue line. These two regions are compatible

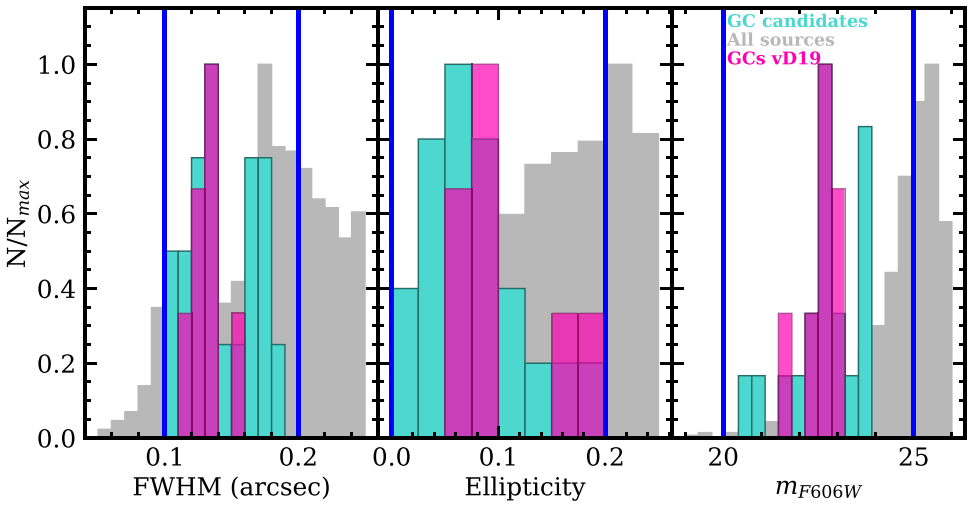

Figure 2. Histograms of FWHM (left), ellipticity (middle), and F606W magnitude m_{F606W} (right) for all the sources simultaneously detected sources in the HST and HiPERCAM images (gray). The magenta histograms show the distribution of the spectroscopically confirmed GCs in vD19. The blue vertical lines mark the range in each parameter of the initial selection. The mint green histograms show the sources that simultaneously satisfy the conditions of FWHM, ellipticity, and magnitude enclosed by the vertical blue lines.

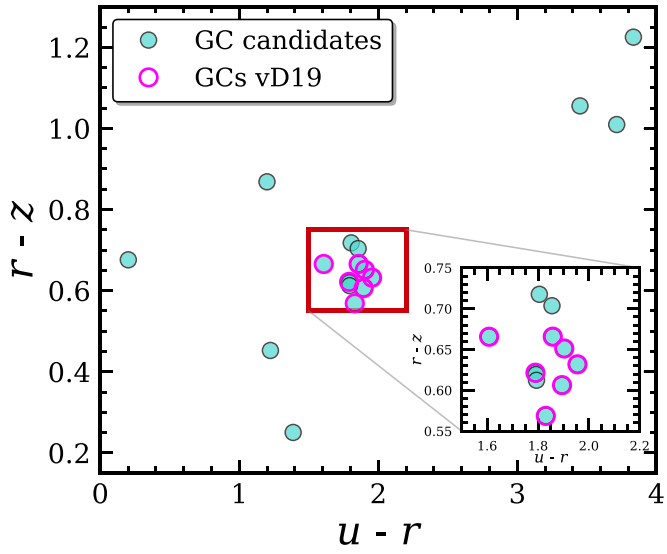

Figure 3. The $(u - r)$–$(r - z)$ color–color diagram of the initial sample of candidate GCs (mint green). The spectroscopically confirmed GCs of vD19 are highlighted in magenta. The red box indicates the color–color region we have selected to create our final sample of GC candidates. The inset shows a zoom-in into the red box for ease of viewing.

given the small number of sources. They are also compatible with the range of axes calculated if only using the confirmed GCs in vD19. The angles defined by these axes and their errors, derived from the slopes of the orthogonal distance regressions, can be found in Table 2.[9]

Consequently, the nonisotropic distribution of GCs around NGC 1052-DF4 is suggesting that it might be experiencing tidal interaction with a neighboring galaxy.

4. Tidal Stripping of the Stellar Distribution

While the study of the spatial distribution of the GCs in NGC 1052-DF4 can provide insights into whether the galaxy is undergoing tidal stripping, the strongest evidence is contained in the outermost part of the object. In fact, in the case of a tidal stripping event, the stellar distribution of NGC 1052-DF4 is expected to be distributed following a characteristic S shape (e.g., Johnston et al. 2002; Klimentowski et al. 2009). We explore this using the IAC80 ultradeep imaging.

4.1. Removal of NGC 1035

Figure 1 already shows that the presence of an excess of light around NGC 1052-DF4 is evident. This excess is centered around the galaxy and has the characteristic S shape of an object undergoing tidal stripping (e.g., Johnston et al. 2002). In order to study how this light is distributed, it is crucial to remove possible contaminants that can bias our results. In Section 2.2.3, we have already modeled and subtracted the bright stars in the field of view, including the nearest star to the west of NGC 1052-DF4. However, even though NGC 1035 is $\sim 4'$ away, the faint halo of this galaxy can contaminate the light of NGC 1052-DF4 in very deep observations.

In order to eliminate this source of contamination, we modeled the galaxy using `ellipse` and `bmodel` in IRAF. While `ellipse` fits elliptical isophotes to the image, `bmodel` uses its output to create a 2D model of the galaxy. The advantage is that the ellipticity and position angle can vary at different radius, achieving a more authentic model of the galaxy and minimizing the residuals.

Prior to using `ellipse`, we need to carefully mask foreground and background sources to reduce contamination that can affect the fitting procedure. As a single `SExtractor` setup for the detection and masking in deep observations is not appropriate, we used a two-step approach: a "hot+cold" mode (e.g., Rix et al. 2004; Montes & Trujillo 2014). The "cold" mode will mask extended sources, while the "hot" mode is optimized to detect the more compact and faint sources that are embedded within the galaxy light.

`SExtractor` was run in a deep combined $g + r + i$ image, and both masks were built from the generated segmentation maps. In the case of the "hot" mode, we unsharp-masked the original image in order to facilitate the masking of the dusty lanes of the galaxy. To create this

[9] Removing C-6, identified as a star in Shen et al. (2020), does not change the results.

Table 1
Confirmed and Candidate GCs of NGC 1052-DF4

Name	R.A.	Decl.	m_u (mag)	m_g (mag)	m_r (mag)	m_z (mag)	m_{F606W} (mag)	m_{F814W} (mag)
C-1[a]	$2^h39^m14\overset{s}{.}52$	$-8°08'27\overset{''}{.}56$	25.69 ± 0.19	24.35 ± 0.03	23.88 ± 0.04	23.17 ± 0.08	23.78 ± 0.02	23.46 ± 0.02
C-2[b]	$2^h39^m16\overset{s}{.}96$	$-8°08'04\overset{''}{.}35$	25.00 ± 0.10	23.49 ± 0.01	23.04 ± 0.02	22.41 ± 0.04	22.93 ± 0.01	22.55 ± 0.01
C-3[b]	$2^h39^m18\overset{s}{.}22$	$-8°07'23\overset{''}{.}17$	24.40 ± 0.06	22.97 ± 0.01	22.50 ± 0.01	21.84 ± 0.02	22.45 ± 0.01	22.06 ± 0.01
C-4[b]	$2^h39^m17\overset{s}{.}23$	$-8°07'05\overset{''}{.}75$	24.47 ± 0.06	23.12 ± 0.01	22.68 ± 0.01	22.06 ± 0.03	22.63 ± 0.01	22.24 ± 0.01
C-5[b]	$2^h39^m15\overset{s}{.}24$	$-8°06'57\overset{''}{.}94$	23.74 ± 0.03	22.34 ± 0.01	21.91 ± 0.01	21.34 ± 0.02	21.70 ± 0.01	21.25 ± 0.01
C-6[c]	$2^h39^m14\overset{s}{.}39$	$-8°06'59\overset{''}{.}81$	23.74 ± 0.03	22.38 ± 0.01	21.95 ± 0.01	21.33 ± 0.01	21.87 ± 0.01	21.48 ± 0.01
C-7[b]	$2^h39^m15\overset{s}{.}21$	$-8°06'52\overset{''}{.}24$	24.88 ± 0.09	23.45 ± 0.01	22.99 ± 0.02	22.38 ± 0.04	22.88 ± 0.01	22.40 ± 0.01
C-8	$2^h39^m16\overset{s}{.}34$	$-8°06'44\overset{''}{.}37$	25.53 ± 0.16	24.24 ± 0.03	23.73 ± 0.03	23.12 ± 0.08	23.66 ± 0.02	23.25 ± 0.01
C-9[b]	$2^h39^m12\overset{s}{.}52$	$-8°06'40\overset{''}{.}50$	24.38 ± 0.06	22.99 ± 0.01	22.53 ± 0.01	21.85 ± 0.02	22.46 ± 0.01	22.04 ± 0.01
C-10	$2^h39^m10\overset{s}{.}55$	$-8°05'45\overset{''}{.}92$	24.53 ± 0.06	23.23 ± 0.01	22.67 ± 0.01	21.97 ± 0.03	22.67 ± 0.01	22.27 ± 0.01
C-11[b]	$2^h39^m16\overset{s}{.}79$	$-8°06'15\overset{''}{.}91$	22.00 ± 0.01	21.12 ± 0.01	20.39 ± 0.01	19.73 ± 0.01	22.35 ± 0.01	21.92 ± 0.01

Notes.
[a] This candidate might be associated to NGC 1052-DF5.
[b] GC spectroscopically confirmed in vD19.
[c] This candidate has been identified as a star in Shen et al. (2020).

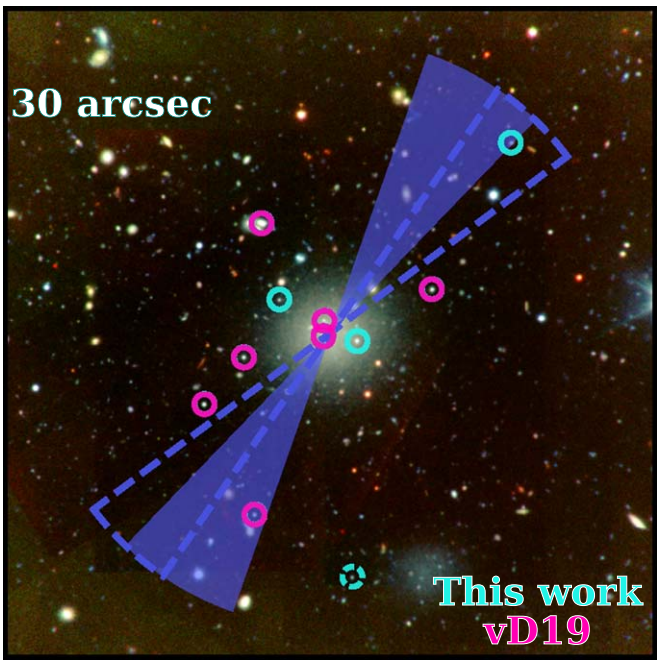

Figure 4. HiPERCAM postage stamp of 240″ × 240″ around NGC 1052-DF4. The mint green circles highlight the candidate GCs found in this work while the magenta circles are the GCs found in vD19. The dashed mint circle at the bottom points to a GC probably associated with NGC 1052-DF5. The blue area indicates the range of directions of the orbit of NGC 1052-DF4 defined by the spatial distribution the GCs. The area enclosed by the dashed blue line is the same but removing the GC probably associated with NGC 1052-DF5 (dashed mint circle). In this image, 30″ corresponds to a distance of ∼2 kpc at a distance of 13.5 Mpc and 2.9 kpc at 20 Mpc.

Table 2
Angles and the Errors of Their Axes Defined by the Spatial Distribution of the GCs of NGC 1052-DF4

	Angle ± Error
All the GCs in this work	58 ± 12
Removing DF5's GC	46 ± 9
Confirmed GCs in vD19	50 ± 18

Note. These angles are defined from the *X*-axis counterclockwise.

unsharp-masked image, we convolved the image with a box filter with a side of 6 pixels and then subtracted it from the original. The "cold" mask was further expanded by 6 pixels while the "hot" was expanded by 3 pixels. Both masks were combined to create the final mask for our IAC80 images, unmasking NGC 1035 on the "cold" mask. This guarantees that the dust lanes and other sources within the galaxy are masked but not the diffuse stellar light of NGC 1035. The final mask was visually inspected to manually mask any remaining light that was missed by the process described above.

We run `ellipse` in the deep $g + r + i$ image in two steps. In the first run, all of the parameters were allowed to vary freely, while in the second run, we fixed the center of the galaxy to the median centers returned in the first run. The geometry of the ellipses obtained in the fitting of the deep image was then used to measure the individual g, r, and i images and create a model of the galaxy using `bmodel`.[10] The fit performed by `ellipse` reaches down to ∼3′ from the center of NGC 1035.

Figure 5 shows the result of subtracting both the light of NGC 1035 and the nearest bright star toward the west of the image. The S shape of the light around NGC 1052-DF4 becomes even more conspicuous after subtracting possible contaminants.

4.2. Surface Brightness Radial Profiles of NGC 1052-DF4

The goal of this paper is to investigate whether NGC 1052-DF4 is interacting with NGC 1035 and if that could explain the lower content of DM in this ultradiffuse galaxy. The presence of tidal tails and other asymmetries that indicate interactions will appear as an excess of light at large radius and deviations from the morphology of the inner parts of the galaxy. To that end, we derived the radial profiles for the IAC80 images using the software `ellipse` in IRAF. `ellipse` fits elliptical isophotes to the 2D images of galaxies using the method described in Jedrzejewski (1987). It provides the median intensity, ellipticity, and position angle for each of the fitted isophotes.

We used the same methodology as in the previous section to build the mask for fitting NGC 1052-DF4. We run

[10] The results of the fit are consistent if we model each band separately.

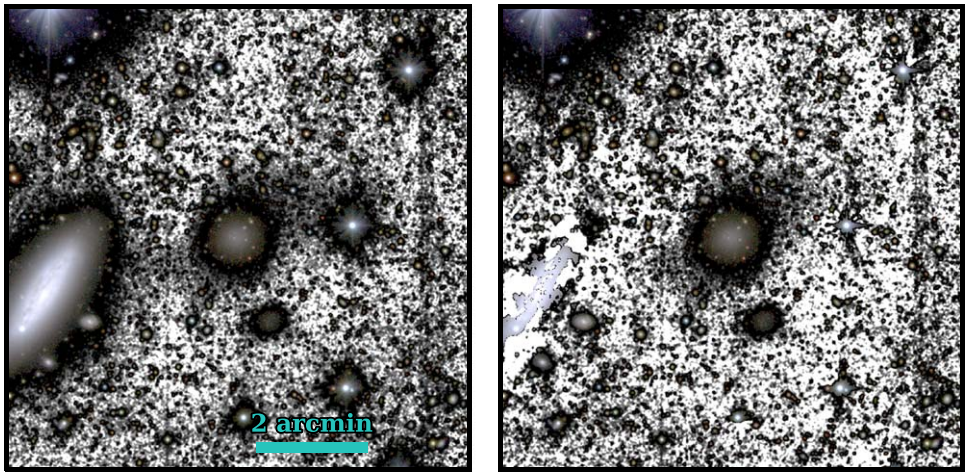

Figure 5. Left panel shows the original IAC80 postage stamp of the 500″ × 500″ region around NGC 1052-DF4. The right panel shows the results of subtracting the nearest bright star (west) and the fitting and removal of NGC 1035. After subtracting these sources of contamination, the S shape of the galaxy becomes more evident.

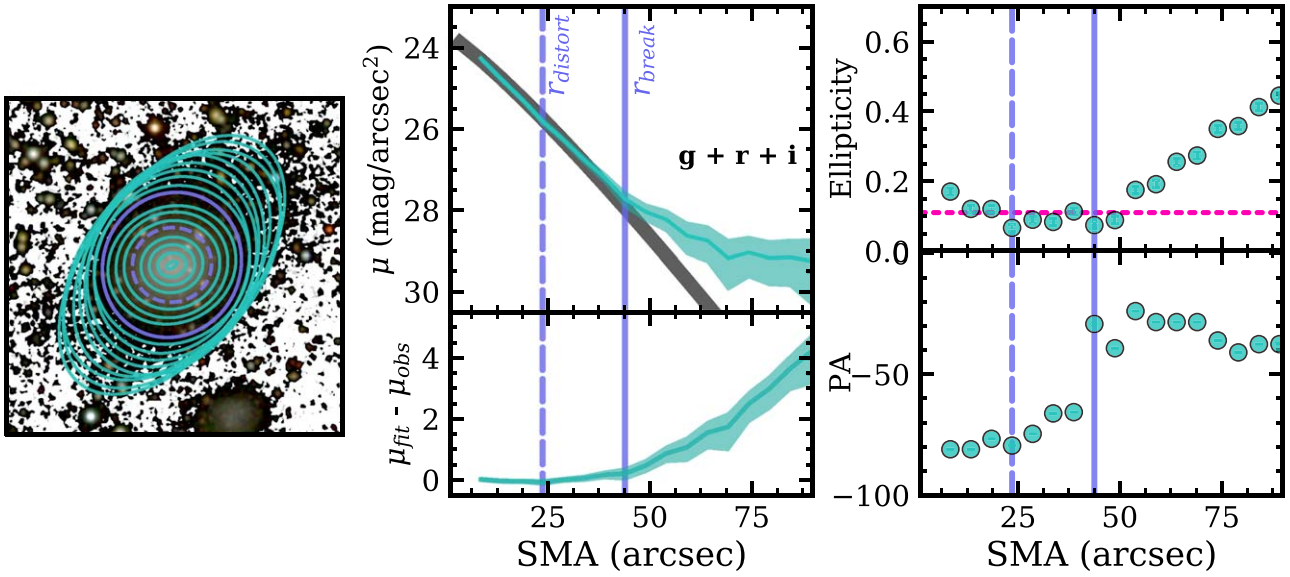

Figure 6. Output from `ellipse` for the $g + r + i$ image of NGC 1052-DF4. The left panel shows the 200″ × 200″ region around NGC 1052-DF4 with the fitted ellipses overplotted. The middle panel shows the radial surface brightness profile as a function of the semimajor axis (top) and the residuals from fitting this profile with a Sérsic model (bottom). The rightmost panel presents the profiles of ellipticity (top) and PA (bottom).

`SExtractor` in the deep $g + r + i$ image and obtain the segmentation maps to build the masks. In this case, the "hot" model was run in the original $g + r + i$ image. The "cold" mask was further expanded by 5 pixels while the "hot" was expanded by 3 pixels, and NGC 1052-DF4 was left unmasked on the "cold" mask. That leaves the light of the galaxy unmasked while masking all compact sources like background galaxies and GCs that are superposed.

Once we have all contaminant sources masked, we derived the radial profiles for the IAC80 $g + r + i$ image with `ellipse`. This image was smoothed with a Gaussian of $\sigma = 2$ pix to improve the signal-to-noise ratio of the outer parts of the galaxy. The isophote fitting process was done in two steps: (1) allowing all parameters to vary freely and (2) fixing the centers to the median centers of the isophotes returned by the first iteration. The `ellipse` geometry obtained was then used to extract the photometry from the original $g + r + i$ image (no smoothing applied) and for each of the individual bands.

Figure 6 shows the output of `ellipse` for the original $g + r + i$ image. In the leftmost panel, a postage stamp of a 200″ × 200″ region around NGC 1052-DF4 is shown with the fitted ellipses overplotted. The 1D radial surface brightness profile as a function of the semimajor axis (SMA) is shown in the top middle panel, up to ∼90″. The shaded regions represent the rms error in each elliptical isophote. The right panel shows the ellipticity (top) and PA (bottom) as a function of SMA. The magenta dashed line in the ellipticity profile marks the value of the ellipticity of NGC 1052-DF4 as reported in vD19. The profiles for each of the individual bands are shown in the Appendix.

4.3. Defining r_{break} and $r_{distort}$ in NGC 1052-DF4

One of the most striking features in the 1D surface brightness profile of NGC 1052-DF4 is its sudden change in the slope at SMA ∼45″. In order to investigate this, Figure 6 also shows a Sérsic (1968) fit to the 1D surface brightness profile of NGC 1052-DF4 (gray line in the top middle panel). This Sérsic

model ($R_e = 18''$ and[11] $n = 0.86$) nicely fits the inner ($R < 40''$) parts of the galaxy, as mentioned in vD19, while at large radius, it is not a good description of the surface brightness profile. The bottom middle panel shows the residuals of subtracting the best Sérsic fit from the $g + r + i$ surface brightness. At a radius of $\sim 45''$, there is a significant excess of light with respect to the model fit. Although this excess starts earlier, the slope of these residuals at this radius becomes steeper. This is accompanied by a steep increase in the ellipticity of the isophotes reaching a value of ~ 0.4 at $\sim 90''$. In addition, there is a sudden change in the PA trend.

Following Johnston et al. (2002), we tentatively define the radius where the surface brightness profile of NGC 1052-DF4 departs ($\Delta\mu \gtrsim 0.2$ mag arcsec^{-2}) from the Sérsic model as the break radius ($r_{\rm break}$) marked as the solid vertical blue line in the profiles at $43\farcs8$. We also marked this particular ellipse in the postage stamp (left panel of Figure 6).

Although this break is the most prominent feature in the surface brightness profile, the satellite starts losing its shape well within this point. Johnston et al. (2002) refers to this point where the morphology of the galaxy is affected by tidal forces as $r_{\rm distort}$. In the case of NGC 1052-DF4, at $\sim 23\farcs5$, the PA starts increasing, i.e., twisting of the isophotes, up to $r_{\rm break}$. This radius is where we define $r_{\rm distort}$, and it is marked in Figure 6 as the dashed blue vertical line in the profiles and the dashed blue ellipse in the postage stamp.

4.4. The S Shape of NGC 1052-DF4

In simulations, tidal debris is seen to spread along the orbit of the satellite in thin streams (e.g., Johnston et al. 1996). This suggests that the morphology of these loose populations can be used to constrain the direction in which the satellite is moving, which in turn can tell us something about the satellite's orbit. In the previous section, we have seen that the change of shape of NGC 1052-DF4 with radius in the $g + r + i$ image suggests that the outer parts of this galaxy are fully compatible with being tidally disrupted (Section 4.3). In order to assess if signs of this interaction can be seen in the individual images, we binned 4 pix × 4 pix the IAC80 images to improve the signal-to-noise ratio of the faint outer parts of the galaxy. Consequently, the new pixel is the sum of 16 original pixels. In addition, we convolved the images with a Gaussian kernel of $\sigma = 1$ (rebinned) pix to further enhance structures. Figure 7 shows the postage stamps of the $250'' \times 250''$ region centered on NGC 1052-DF4 of the three bands: g (left), r (middle), and i (right).

In each of the images, there is an excess of light around NGC 1052-DF4 aligned with the range of orbit direction derived from the distribution of GCs in Section 3.2, overplotted on the g-band stamp (left), that is, to the northwest and southeast of the galaxy, marked by the teal arrows in the rightmost panel of Figure 7. This excess is seen in all three bands independently. By confirming the presence of this excess in the three different bands, we ensure that it is a real feature.

To explore in more detail this observed S shape and therefore constrain the direction in which NGC 1052-DF4 is moving, we derived the isocontours of the light of this galaxy. To do that, we use the rebinned IAC80 $g + r + i$ and convolve it with a Gaussian of $\sigma = 2.5$ pix to further enhance structures that might be buried in the noise. We constructed a new mask for this image by visually masking all of the sources. In addition, we generously masked the residuals of the star to the west and of NGC 1035.

We derived the isocontours of light using `matplotlib`'s `contour` function in a similar way to Montes & Trujillo (2019). `contour` provides and draws isocontour lines at different given intensities in the image. In this case, we derived the radial light profiles of the binned $g + r + i$ image in elliptical apertures, assuming a fixed ellipticity of 0.11 ($b/a = 0.89$) and PA of 7° (counterclockwise from the X-axis), the properties of the inner parts of the galaxy.[12] Using this radial profile, we interpolated the intensity values at five physical radial distances: $10''$, $20''$, $30''$, $40''$, and $50''$ from the center of NGC 1052-DF4. The different distances correspond to surface brightness values of 24.6, 25.8, 26.9, 27.8, and 29.1 mag arcsec^{-2}. These contours are plotted in Figure 8. In the left panel, the underlying image is a composite of an RGB color image created using the binned (4 × 4) g, r, and i filters and a black and white $g + r + i$ binned image for the background.

On the right panel, we plotted the same contours on a black background to facilitate visualization. We can clearly see that the last contour (lightest teal shade, at 29.1 mag arcsec^{-2}) shows the presence of tidal tails from material moving away from NGC 1052-DF4. Tentatively, we have drawn a schematic S shape (in purple) tracing the shape of this last contour. We also plotted the region containing the axes from the distribution of GCs (Section 3.2). The S shape observed here is common in simulations where a dwarf galaxy is interacting with a more massive galaxy (e.g., Figure 5 in Johnston et al. 2002) and also in observations (e.g., Koch et al. 2012).

4.5. Tidal Radius

The tidal radius identifies the radius where the tidal effects are expected to be important in the satellite. To compute the tidal radius ($r_{\rm tidal}$) for NGC 1052-DF4, we follow Equation (5) in Johnston et al. (2002). This equation is for the tidal radius at the pericenter of the satellite orbit. Instead, as we do not know where NGC 1052-DF4 is in relation to its orbit around NGC 1035, we computed the instantaneous $r_{\rm tidal}$, which is the tidal radius at the current position of the satellite from the parent galaxy and assuming zero ellipticity, i.e., a circular orbit (Johnston et al. 2002). Consequently, the equation for the instantaneous $r_{\rm tidal}$ is given by

$$r_{\rm tidal,inst} = D \times \left(\frac{m_{\rm dyn}}{M_{\rm 1035,dyn}}\right)^{1/3}, \quad (1)$$

where D is the radial distance between the galaxies and $m_{\rm dyn}$ and $M_{\rm 1035,dyn}$ are the dynamical masses for NGC 1052-DF4 and NGC 1035, respectively. The dynamical mass of NGC 1035 is $M_{\rm 1035,dyn} = (1.9 \pm 0.1) \times 10^{10} M_\odot$ (Truong et al. 2017),[13] while for NGC 1052-DF4 we took the estimation of the total mass from vD19; $m_{\rm dyn} = 4^{+12}_{-3} \times 10^7 M_\odot$, assuming a distance of 20 Mpc (see also Danieli et al. 2020). At a distance of

[11] This is 1.2 kpc at 13.5 Mpc or 1.7 kpc at 20 Mpc.

[12] As shown in Figure 1 of Montes & Trujillo (2019), the purpose of this is to obtain approximate values at a certain distance in order to derive a contour, and therefore, the real shape of the galaxy light at that distance.

[13] The dynamical mass of NGC 1035 in Truong et al. (2017) was estimated at a distance of 17 Mpc. As the way this dynamical mass was estimated is proportional to the size of NGC 1035, we converted it according to the distance in our calculations.

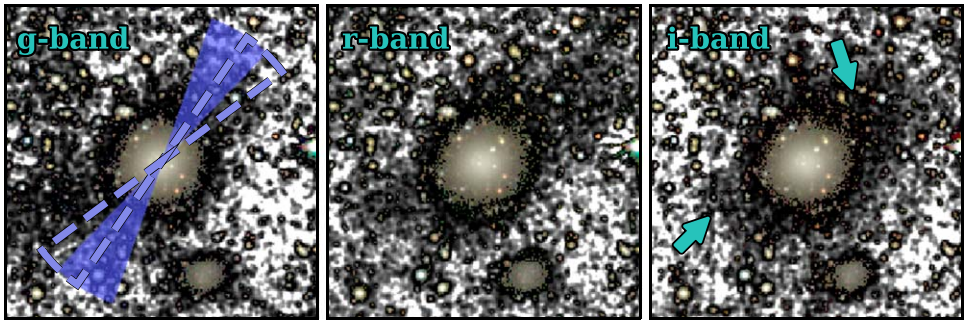

Figure 7. Postage stamps of the 250″ × 250″ region centered on NGC 1052-DF4 for the *g* (left), *r* (middle) and *i* (right) IAC80 images. The blue-shaded region indicates the range of the different directions of the orbit of this galaxy as derived by the spatial distribution of GCs in Section 3.2, overplotted on the *g*-band stamp. The region outlined by the dashed line corresponds to the same range of orbits but without including the GC possibly associated with NGC 1052-DF5. The excess of light to the northwest and southeast of NGC 1052-DF4 is marked by two teal arrows in the rightmost panel (*i* band).

13.5 Mpc, this dynamical mass would be around half of that value. Assuming that the projected distance between the galaxies is the actual distance between their centers, $D = 222''$, we obtained $r_{\rm tidal} = 33 \pm 8''$ and $28 \pm 12''$, depending on the distance assumed, 13.5 and 20 Mpc, respectively.

This is similar to the $r_{\rm distort}$ identified in Figure 6 (23.5″). $r_{\rm distort}$ is defined as the radius where the morphology of the galaxy departs from its original shape. In this case, at $r_{\rm distort}$, the PA of the isophotes starts increasing, i.e., twisting, marking the point where the tidal forces are starting to affect the morphology of galaxy although the stars still remain bound to the satellite (e.g., Peñarrubia et al. 2009).

Note that if NGC 1052-DF4 was located at 20 Mpc (Danieli et al. 2020), the most likely disturber would be NGC 1052. Assuming the following dynamical mass for NGC 1052 $M_{1052,\rm dyn} = (1.7 \pm 0.9) \times 10^{12} M_{\odot}$ (at 18 Mpc; Pierce et al. 2005) and a distance of 28.′7 between both galaxies, we obtain a tidal radius of $51 \pm 15''$. This is around twice larger than if we assume NGC 1035 is the main galaxy responsible for the tidal distortion of NGC 1052-DF4. This larger value for the tidal radius would be in tension with the $r_{\rm distort}$ measured in this paper. This suggests that NGC 1035 is likely responsible for the disruption of NGC 1052-DF4.

4.6. Stellar Mass in the Tidal Tails

$r_{\rm break}$ identifies the radius where observations become dominated by the unbound populations of stars and therefore where we can find breaks in the light profiles (e.g., Johnston et al. 2002; Peñarrubia et al. 2009). The lack of strong distortions in the stellar light at the center of NGC 1052-DF4 indicates that the stars of this galaxy might only be starting to be stripped now. Consequently, we can infer a lower limit to the amount of stellar mass stripped so far by NGC 1052-DF4 by measuring the stellar mass outside $r_{\rm break}$. The fraction of the stellar light of NGC 1052-DF4 beyond $r_{\rm break}$, including the tidal tails down to $\mu_r = 29.1$ mag arcsec^{-2}, is 7±1%, averaging the individual estimates from the *g*, *r* and *i* bands. This relatively low value for the stripped stellar mass, together with the fact that the central part of the galaxy appears undisturbed, is compatible with the idea that the stellar body of the galaxy is only starting to be disrupted now. Note that this quantity is a lower limit of the true fraction of mass lost by the galaxy.

5. Discussion

In this work, we show that NGC 1052-DF4 presents clear signs of interaction. In the following, we discuss how this interaction can affect the amount of DM present in this galaxy. For all the calculations, we assume that the distance to the galaxy is 13.5 Mpc (Monelli & Trujillo 2019), although qualitatively the main results presented here do not depend on this assumption.

Note that the previous deep imaging of NGC 1052-DF4 reached around $\mu_r = 28.5$ mag arcsec^{-2} (3σ, $10'' \times 10''$, Müller et al. 2019), still inconclusive for addressing the problem of the interaction between these two systems. Similarly, the data from The Dragonfly Telephoto Array, where this galaxy was identified (Cohen et al. 2018), reach between $\mu_{g/r} = 27.4$ and 28.0 mag arcsec^{-2} ($3\sigma, 12'' \times 12''$) as reported in Merritt et al. (2016).

5.1. The Distribution of Light and GCs of NGC 1052-DF4

Matter stripped from satellite galaxies forms tidal tails which will eventually become completely unbound and form larger tidal extensions tracing approximately the original orbit of the satellite in its host halo. In the same manner, the GCs of these satellites will be stripped from the galaxy and deposited along the orbit.

Using *N*-body simulations, Klimentowski et al. (2009) studied the properties of tidal tails of a dwarf galaxy orbiting in a Milky Way-like potential. They showed that there are always two tidal tails emanating from the two opposite sides of the dwarf galaxy and that, for most of the time, these tails are oriented radially toward the host galaxy and not along the orbit. This shape, reminiscent of an S, is produced by the particles that, once unbound, are seen to move in the direction of the tidal forces, which are perpendicular to the orbit of the satellite, before being dispersed along it.

The outskirts of NGC 1052-DF4 present an excess of light to the northwest and southeast of the galaxy (marked by arrows in Figure 7). In Figure 8, we explored this in more depth using a binned $g + r + i$ and plotting isocontours of light at different surface brightness values. The faintest surface brightness (29.1 mag arcsec^{-2}) clearly shows an S shape (tentatively drawn in purple). The tails of the S are oriented directly to NGC 1035 (see Figure 1), indicating that this disk galaxy (Truong et al. 2017) is causing the tidal perturbation. As shown in Figure 5 in Monelli & Trujillo (2019), NGC 1035 is the closest galaxy to NGC 1052-DF4 at a projected distance of

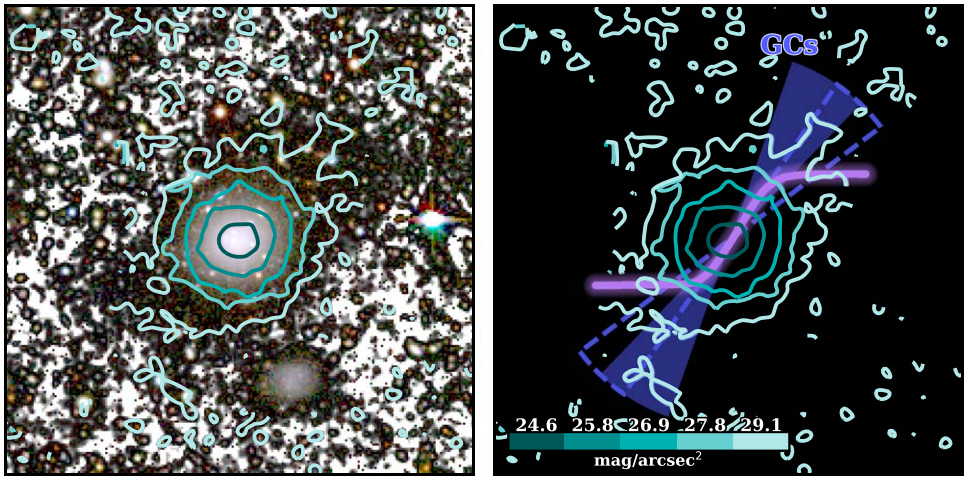

Figure 8. Contours at five different surface brightness levels of NGC 1052-DF4. The left panel shows the contours overplotted on a composite from an RGB color image and a black and white $g + r + i$ image for the background. The images are 4×4 binned. The right panel shows the contours over a black background with a tentative S shape (purple solid line) tracing the shape of the last contours (at 29.1 mag arcsec^{-2}). We also plotted the range of directions of the orbit of this galaxy obtained from the GC distribution (blue solid area) and without the GC probably associated with NGC 1052-DF5 (dashed line) in Section 3.2. The S shape is compatible with NGC 1052-DF4 moving along the direction defined by the position of the GCs.

$\sim 222'' = 14.5$ kpc, at a distance of 13.5 Mpc (Sorce et al. 2014; Monelli & Trujillo 2019).

In addition, in Section 3.2, we identify four new GC candidates of NGC 1052-DF4. These, along with the confirmed GCs in vD19, align in a particular direction. This preferential alignment of the GCs suggests that they are also being stripped in the interaction, and therefore, they are distributing in the direction of the orbit.

Putting all the evidence together, what Figure 8 is telling us is that NGC 1052-DF4 is moving roughly along the direction defined by the axis of the GCs, roughly perpendicular to the tails of the S.

5.2. Can Tidal Stripping Explain the Missing Dark Matter in NGC 1052-DF4?

Deep imaging of NGC 1052-DF4 has revealed that this galaxy is undergoing tidal disruption. Now, the question that arises is whether this tidal interaction could explain the low DM content measured in this galaxy.

Smith et al. (2013, 2016) used numerical simulations to explore the effect of tidal stripping in the DM content of dwarf galaxies in clusters of galaxies. They found that only when the remaining DM fraction falls under 10%–15% is when the stars and GCs of the galaxy are significantly stripped. We warn the reader that these simulations cannot be directly compared to the NGC 1052-DF4 scenario, but they provide a qualitative understanding of the problem.

To assess whether the tidal stripping scenario explains the properties of NGC 1052-DF4, we need to calculate the remaining fraction of DM. For this, we first determined the total stellar mass of the galaxy (including tidal tails). The colors were obtained by integrating the light of the galaxy and tidal tails for each of the bands, g, r, and i. We used the relations between color and mass-to-light ratios from Roediger & Courteau (2015) for three combinations of colors $g - r$, $g - i$, and $r - i$. The total stellar mass of the galaxy is $M_* = (3.6 \pm 1.3) \times 10^7 M_\odot$, the average and dispersion from the three individual estimates, at 13.5 Mpc.

Using the stellar mass to halo mass relationship in Brook et al. (2014), we derived an expected initial total mass for NGC 1052-DF4 of $M_{h,\mathrm{ini}} = (2.2 \pm 0.3) \times 10^{10} M_\odot$.[14] Taking the current estimate of the total dynamical mass measured in vD19, the average remaining fraction of DM of $\lesssim$1%. However, the dynamical mass-to-light ratios of isolated UDGs vary widely (e.g., Toloba et al. 2018; Müller et al. 2020), affecting our estimate of the initial total mass of the galaxy. So, the remaining DM fraction could be as high as 10%.

This is consistent with the simulations in Smith et al. (2013, 2016). The bulk of the stars in a satellite are located in the very central regions of its DM halo. Hence, the stars are more shielded from the tidal forces of the host galaxy with respect to the outer parts of the DM halo. This means that, during the interaction, the DM from the outer parts will be preferentially stripped over the stars of the galaxy (Smith et al. 2016). In other words, the mass stripping of DM halos proceeds gradually from the outside in (e.g., Stoehr et al. 2002; Peñarrubia et al. 2008; Smith et al. 2016).

In NGC 1052-DF4, the fraction of stellar mass in the tidal tails is $\sim$7% (Section 4.6), meaning that the bound stellar mass is 93%, in contrast with the $\lesssim$1% of DM still bound to the galaxy. This indicates that the galaxy has lost significant amounts of DM before it started losing its stars, in agreement with simulations.[15] Therefore, tidal stripping is a very likely explanation for the extremely low DM content of NGC 1052-DF4 (see also Ogiya 2018; Jackson et al. 2020; Łokas 2020; Macciò et al. 2020; Nusser 2020; Yang et al. 2020).

Note that we are assuming that the measured DM content of this galaxy in vD19 is not affected by the tidal interaction. According to Smith et al. (2013), the observed GC velocity dispersion can be used to measure the true enclosed total mass to within a factor of 2, even when the remaining DM fraction falls as low as $\sim$3%. However, when it drops below 3%, the total mass is overestimated due to the presence of large

[14] Alternatively, if we use the number of GCs to infer the initial halo mass of this galaxy as in Saifollahi et al. (2020), the result is $M_{h,\mathrm{ini}} = 3.6 \times 10^{10} M_\odot$ for the seven confirmed GCs in vD19 or $M_{h,\mathrm{ini}} = 5.6 \times 10^{10} M_\odot$ for all the GCs identified in this work, a factor of 1.8–2.5 higher.

[15] Even if the fraction of stellar mass unbound was of 50% of the current stellar mass of the galaxy, this scenario will still be true.

numbers of unbound GCs that boost the inferred velocity dispersion of the system (Smith et al. 2013).

To sum up, the preferential tidal stripping of DM over the stars in NGC 1052-DF4 is a very plausible explanation for the measured low content of DM in this galaxy.

6. Conclusions

The recent discovery of a second galaxy "missing" dark matter had the potential to revolutionize how we understand galaxy formation. In this work, we have shown evidence that this galaxy is undergoing tidal disruption. Therefore, the "absence of dark matter" in NGC 1052-DF4 is almost certainly caused by its interaction with its neighbor, NGC 1035. Dark matter is less concentrated than stars and, therefore, during interactions, is preferentially stripped from satellite galaxies. In the case of NGC 1052-DF4, as the central parts of the galaxy remain untouched and only ∼7% of the stellar mass of the galaxy is in the tidal tails, we can assume that the stellar component is now starting to be stripped.

This work shows the necessity of very deep imaging in order to detect and characterize these faint substructures around dwarf satellites in nearby galaxies in order to explain peculiarities that, otherwise, remain inexplicable in shallower data.

We would like to thank the anonymous referee for their comments that helped to improve the manuscript. M.M. thanks Sarah Brough for many useful discussions while preparing this manuscript. We acknowledge support from grant PID2019-107427GB-C32 from the Spanish Ministry of Science and Innovation. We acknowledge financial support from the European Union's Horizon 2020 research and innovation program under Marie Skłodowska-Curie grant agreement No. 721463 to the SUNDIAL ITN network and the European Regional Development Fund (FEDER), from IAC project P/300624, financed by the Ministry of Science, Innovation and Universities, through the State Budget and by the Canary Islands Department of Economy, Knowledge and Employment, through the Regional Budget of the Autonomous Community, and from the Fundación BBVA under its 2017 program of assistance to scientific research groups, for the project "Using machine-learning techniques to drag galaxies from the noise in deep imaging." J.R. acknowledge financial support from grants AYA2015-65973-C3-1-R and RTI2018-096228-B-C31 (MINECO/FEDER, UE), as well as from the State Agency for Research of the Spanish MCIU through the "Center of Excellence Severo Ochoa" award to the Instituto de Astrofísica de Andalucía (SEV-2017-0709). A.B. was supported by an appointment to the NASA Postdoctoral Program at the NASA Ames Research Center, administered by Universities Space Research Association under contract with NASA. Based on observations made with the GTC telescope, in the Spanish Observatorio del Roque de los Muchachos of the Instituto de Astrofísica de Canarias, under Director's Discretionary Time.

Facilities: HST(ACS), GTC, IAC80.

Software: Astropy (The Astropy Collaboration et al. 2018), `SExtractor` (Bertin & Arnouts 1996), `SCAMP` (Bertin 2006), `SWarp` (Bertin 2010), Gnuastro (Akhlaghi & Ichikawa 2015), `photutils` v0.7.2 (Bradley et al. 2019), `pillow` (van Kemenade et al. 2020), `ellipse` (Jedrzejewski 1987), numpy (Oliphant 2006), scipy (Virtanen et al. 2020), Astrodrizzle (Gonzaga et al. 2012), Astrometry.net (Lang et al. 2010).

Appendix
Surface Brightness Profiles of the IAC80 Images

Figure 9 shows the individual surface brightness profiles derived with `ellipse` for the IAC80 *g*, *r*, and *i* bands (top panels). The lower panels show the residuals of fitting a Sérsic (1968) model to the profile of the galaxy (gray thick line in the

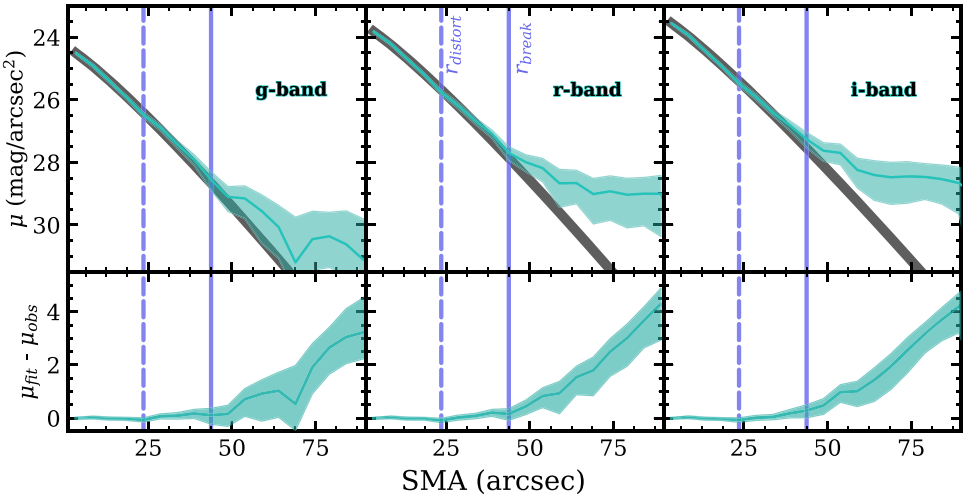

Figure 9. 1D radial surface brightness profiles of the IAC80 images in the *g* (left), *r* (middle), and *i* bands. The lower panels show the residual from fitting the corresponding profile with a Sérsic model. There is an excess of light beyond ∼45″ in all bands.

top panels). The details of the fitting procedure are given in Section 4.2.

ORCID iDs

Mireia Montes https://orcid.org/0000-0001-7847-0393
Raúl Infante-Sainz https://orcid.org/0000-0002-6220-7133
Alberto Madrigal-Aguado https://orcid.org/0000-0002-9510-0893
Javier Román https://orcid.org/0000-0002-3849-3467
Matteo Monelli https://orcid.org/0000-0001-5292-6380
Alejandro S. Borlaff https://orcid.org/0000-0003-3249-4431
Ignacio Trujillo https://orcid.org/0000-0001-8647-2874

References

Aihara, H., Armstrong, R., Bickerton, S., et al. 2018, PASJ, 70, S8
Akhlaghi, M. 2019, arXiv:1909.11230
Akhlaghi, M., & Ichikawa, T. 2015, ApJS, 220, 1
Akhlaghi, M., Infante-Sainz, R., Roukema, B. F., Valls-Gabaud, D., & Baena-Gallé, R. 2020, arXiv:2006.03018
Alam, S., Albareti, F. D., Allende Prieto, C., et al. 2015, ApJS, 219, 12
Bertin, E. 2006, in ASP Conf. Ser. 351, Astronomical Data Analysis Software and Systems XV, ed. C. Gabriel et al. (San Francisco, CA: ASP), 112
Bertin, E. 2010, SWarp: Resampling and Co-adding FITS Images Together, Astrophysics Source Code Library, ascl:1010.068
Bertin, E., & Arnouts, S. 1996, A&AS, 117, 393
Borlaff, A., Trujillo, I., Román, J., et al. 2019, A&A, 621, A133
Bradley, L., Sipocz, B., Robitaille, T., et al. 2019, astropy/photutils: v0.7.1, Zenodo, doi:10.5281/zenodo.3478575
Brodie, J. P., & Strader, J. 2006, ARA&A, 44, 193
Brook, C. B., Di Cintio, A., Knebe, A., et al. 2014, ApJL, 784, L14
Cohen, Y., van Dokkum, P., Danieli, S., et al. 2018, ApJ, 868, 96
Danieli, S., van Dokkum, P., Abraham, R., et al. 2020, ApJL, 895, L4
Dhillon, V., Dixon, S., Gamble, T., et al. 2018, Proc. SPIE, 10702, 107020L
Duc, P. A., Brinks, E., Springel, V., et al. 2000, AJ, 120, 1238
Forbes, D. A. 2017, MNRAS, 472, L104
Freeman, K. C. 1970, ApJ, 160, 811
Gonzaga, S., Hack, W., Fruchter, A., & Mack, J. 2012, The DrizzlePac Handbook (Baltimore, MD: STScI)
Goranova, Y., Hudelot, P., Magnard, F., et al. 2009, The CFHTLS T0006 Release, http://terapix.iap.fr/cplt/T0006-doc.pdf
Harris, W. E. 1996, AJ, 112, 1487
Hudson, M. J., & Robison, B. 2018, MNRAS, 477, 3869
Hughes, M. E., Pfeffer, J., Martig, M., et al. 2019, MNRAS, 482, 2795
Infante-Sainz, R., Trujillo, I., & Román, J. 2020, MNRAS, 491, 5317
Jackson, R. A., Kaviraj, S., Martin, G., et al. 2020, arXiv:2010.02219
Jedrzejewski, R. I. 1987, MNRAS, 226, 747
Johnston, K. V., Choi, P. I., & Guhathakurta, P. 2002, AJ, 124, 127
Johnston, K. V., Hernquist, L., & Bolte, M. 1996, ApJ, 465, 278
Klimentowski, J., Łokas, E. L., Kazantzidis, S., et al. 2009, MNRAS, 400, 2162
Koch, A., Burkert, A., Rich, R. M., et al. 2012, ApJL, 755, L13
Lang, D., Hogg, D. W., Mierle, K., Blanton, M., & Roweis, S. 2010, AJ, 139, 1782
Lelli, F., Duc, P.-A., Brinks, E., et al. 2015, A&A, 584, A113
Łokas, E. L. 2020, A&A, 638, 133
Macciò, A. V., Huterer Prats, D., Dixon, K. L., et al. 2020, arXiv:2010.02245
Mackey, A. D., Huxor, A. P., Ferguson, A. M. N., et al. 2010, ApJL, 717, L11
Merritt, A., van Dokkum, P., Abraham, R., & Zhang, J. 2016, ApJ, 830, 62
Monelli, M., & Trujillo, I. 2019, ApJL, 880, L11
Montes, M., Acosta-Pulido, J. A., Prieto, M. A., & Fernández-Ontiveros, J. A. 2014, MNRAS, 442, 1350
Montes, M., & Trujillo, I. 2014, ApJ, 794, 137
Montes, M., & Trujillo, I. 2019, MNRAS, 482, 2838
Müller, O., Marleau, F. R., Duc, P.-A., et al. 2020, A&A, 640, A106
Müller, O., Rich, R. M., Román, J., et al. 2019, A&A, 624, L6
Muñoz, R. P., Puzia, T. H., Lançon, A., et al. 2014, ApJS, 210, 4
Nusser, A. 2020, ApJ, 893, 66
Ogiya, G. 2018, MNRAS, 480, L106
Oliphant, T. E. 2006, A Guide to NumPy, Vol. 1 (USA: Trelgol Publishing)
Peñarrubia, J., Navarro, J. F., & McConnachie, A. W. 2008, ApJ, 673, 226
Peñarrubia, J., Navarro, J. F., McConnachie, A. W., & Martin, N. F. 2009, ApJ, 698, 222
Pierce, M., Brodie, J. P., Forbes, D. A., et al. 2005, MNRAS, 358, 419
Ploeckinger, S., Recchi, S., Hensler, G., & Kroupa, P. 2015, MNRAS, 447, 2512
Ploeckinger, S., Sharma, K., Schaye, J., et al. 2018, MNRAS, 474, 580
Read, J. I., Wilkinson, M. I., Evans, N. W., Gilmore, G., & Kleyna, J. T. 2006, MNRAS, 367, 387
Rix, H.-W., Barden, M., Beckwith, S. V. W., et al. 2004, ApJS, 152, 163
Roediger, J. C., & Courteau, S. 2015, MNRAS, 452, 3209
Román, J., Trujillo, I., & Montes, M. 2019, arXiv:1907.00978
Rubin, V. C., Ford, W., & Kent, J. 1970, ApJ, 159, 379
Saifollahi, T., Trujillo, I., Beasley, M. A., Peletier, R. F., & Knapen, J. H. 2020, arXiv:2006.14630
Sérsic, J. L. 1968, Atlas de Galaxias Australes (Cordoba: Observatorio Astronomico)
Shen, Z., van Dokkum, P., & Danieli, S. 2020, arXiv:2010.07324
Smith, R., Choi, H., Lee, J., et al. 2016, ApJ, 833, 109
Smith, R., Sánchez-Janssen, R., Fellhauer, M., et al. 2013, MNRAS, 429, 1066
Sorce, J. G., Tully, R. B., Courtois, H. M., et al. 2014, MNRAS, 444, 527
Stoehr, F., White, S. D. M., Tormen, G., & Springel, V. 2002, MNRAS, 335, L84
Taylor, M. A., Puzia, T. H., Muñoz, R. P., et al. 2017, MNRAS, 469, 3444
The Astropy Collaboration, Price-Whelan, A. M., Sipőcz, B. M., et al. 2018, arXiv:1801.02634
Toloba, E., Lim, S., Peng, E., et al. 2018, ApJL, 856, L31
Toomre, A., & Toomre, J. 1972, ApJ, 178, 623
Trujillo, I., Beasley, M. A., Borlaff, A., et al. 2019, MNRAS, 486, 1192
Trujillo, I., & Fliri, J. 2016, ApJ, 823, 123
Truong, P. N., Newman, A. B., Simon, J. D., et al. 2017, ApJ, 843, 37
van Dokkum, P., Danieli, S., Abraham, R., Conroy, C., & Romanowsky, A. J. 2019, ApJL, 874, L5
van Dokkum, P., Danieli, S., Cohen, Y., et al. 2018, Natur, 555, 629
van Kemenade, H., wiredfool, Murray, A., et al. 2020, python-pillow/Pillow 7.1.1, Zenodo, doi:10.5281/zenodo.3738618
Virtanen, P., Gommers, R., Oliphant, T. E., et al. 2020, NatMe, 17, 261
Yang, D., Yu, H.-B., & An, H. 2020, PhRvL, 125, 111105